JOURNAL OF MATERIALS SCIENCE 32 (1997) 5085–5099

Dynamics and microstructural evolution of bulk amorphous $Cu_{12.5}Ni_{10}Zr_{41}Ti_{14}Be_{22.5}$ during phase separations: a small-angle neutron scattering approach

JUN-MING LIU
National Laboratory of Solid State Microstructures, Nanjing University and Center for Advanced Studies in Science and Technology of Microstructures, Nanjing 210093, People's Republic of China and Hahn-Meitner-Institut Berlin, Bereich NM, Glienicker Straße 100, 14109 Berlin, Germany

Small-angle neutron scattering has been applied to investigate in detail the structural relaxation of bulk amorphous $Cu_{12.5}Ni_{10}Zr_{41}Ti_{14}Be_{22.5}$ alloy in the supercooled liquid range (620–673 K) and its effect on subsequent crystallization around the crystallization point (673 K). The interference events from typical phase separation were recorded as the alloy was annealed in the supercooled liquid range. It was revealed that the crystallization in the alloy which was previously relaxed in the supercooled liquid range was significantly prohibited, and further phase separation was observed. Considerable temperature dependence of these phase separations was observed. It has been demonstrated that the phase separation developed via the spinodal mode and the achieved microstructure consisted of one droplet-like supercooled liquid phase embedded in the similarly disordered matrix. The droplets showed a bar-like pattern and distributed in a relatively regular form in the matrix. The phase separations exhibited sluggish coarsening kinetics with much smaller exponent than the Lifshitz–Slyozov–Wagner value. However, the dynamic scaling property of the phase separations at different temperatures has been approved by our scaling analysis.

1. Introduction

Metallic glasses are currently produced by rapidly quenching at a rate of at least 10^5 K s^{-1} or from the highly supercooled liquid by the quasistatic processing at slow cooling where the potential heterogeneous nucleation of any crystalline phase is effectively prohibited. These amorphous metallic materials have been paid special attention in the last few decades, not only because they exhibit excellent mechanical and engineering properties and have achieved wide applications, but also as representative examples of fundamental condensed-matter studies [1–6]. Recently, a series of large-size bulk metallic glasses with a complex multicomponent chemistry have been successfully developed by the quasistatic processing [7–11]. These new alloys show high processing capabilities of the supercooled liquid, improved wear resistance, low coefficient of friction, high strength and excellent corrosion resistance. Also sufficient thermal stability against crystallization, characterized by the high glass transition point, T_g, and wide supercooled liquid range before crystallization, is achieved in these alloys. Therefore, intensive research activities on these new alloys have been stimulated in the last few years [10, 11].

Amorphous $Cu_{12.5}Ni_{10}Zr_{41}Ti_{14}Be_{22.5}$ is a representative of these alloys [12–14]. An amorphous ingot of this alloy 20 mm in size can be easily processed at a cooling rate of about 10 K s^{-1}. This alloy exhibits a high glass-forming ability and the improved properties mentioned above and thus has attracted special interest from materials scientists in the last two years. Some interesting phenomena associated with the structural relaxation and crystallization in this alloy have been revealed [15–20]. This alloy shows a supercooled liquid range (SLR) approximately 60 K wide above its $T_g \approx 615$–618 K, determined by differential scanning calorimetry (DSC) [17]. Depending on the thermal history it acquired different microstructures consisting of nano-sized crystals embedded in a single-phase or multiphase matrix of the supercooled liquid state. The microstructure achieved on heating to a temperature higher than the crystallization point, T_x, after a full relaxation in the SLR might be significantly different from that obtained if the relaxation is avoided. In particular, crystallization in the relaxed alloy was found to be considerably prohibited. Some peculiar behaviours of element diffusion on passing through the SLR were also revealed, and they were postulated to be related to the structural relaxation. It

0022–2461

has been widely believed that structural relaxation in the SLR for this alloy affects significantly microstructure eventually formed and the subsequent crystallization.

The preliminary studies of structural relaxation in the SLR of this alloy revealed a phase separation sequence. This phenomenon in the supercooled liquid state has previously been reported for the systems Ti–Zr–Be, Zr–Cu, Zr–Co, La–Ni–Al, etc. [21–24]. To date, a series of techniques, including transmission electron microscopy (TEM) [18, 19], atom-probe field ion microscopy (APFIM) [14, 19], secondary ion mass spectrometry (SIMS) [15, 25] and small-angle neutron scattering (SANS) [18, 20] have been applied to investigate the phase separation and related diffusion in the SLR of $Cu_{12.5}Ni_{10}Zr_{41}Ti_{14}Be_{22.5}$, with the emphasis on its microstructural evolution and kinetic mechanism. The results achieved in several publications seems to lead to contradictory arguments. The TEM observations of Macht *et al.* [19] revealed that the amorphous sample annealed in the SLR reflected the electron beam with two diffraction rings which were separated from each other and also the dark-field image exhibited visible contrast arising from the nano-sized clusters of one phase embedded in the matrix, both of which were disordered. However, similar checking by Schneider *et al.* [18] showed the formation of nano-sized crystals embedded in the amorphous matrix for a long period of annealing in the SLR. The SANS measurements by Wiedenmann *et al.* [20] detected a distinct peak in the scattering curve and a "peak shift" towards the low-wave vector range as long as the sample was in the SLR and the microstructure was still disordered. In the SANS investigation by Schneider *et al.* [18] a discernible scattering intensity was obtained only after the sample had been annealed in the SLR for a period of time, i.e., there existed an incubation period during which phase separation occurred and led to formation of nanocrystals. This incubation time was, for example, about 100 min at $T = 623$ K. For the latter study it was concluded that the phase separation in the SLR destabilizes the supercooled liquid state against crystallization, which contradicts the argument of Wiedenmann *et al.* [20].

The composition fluctuations during the phase separation was probed with APFIM [19], which presented direct evidence that anticorrelated fluctuations of Ti and Be exist, although the real constitution of the products of the phase separation has still not been determined. The wavelength of the fluctuations was about several to more than 10 nm. Similarly, the diffusion measurements by means of SIMS [15, 25] revealed anomalous diffusion behaviours for Be, Al and Co during the phase separation and we may expect similar behaviours for Zr, Ti and Ni. Typically, Be showed fast diffusion whereas the other elements showed a continuous decrease in their diffusivity with time.

Another fact about this alloy is the very sluggish kinetics in the late stage of the phase separation. Previous observations claimed that the process in fact ceased after about several hours [20]. This phenomenon is obviously related to the anomalous behaviours of the species diffusion and the extremely high stability of the products of the phase separation, with the specific mechanism remaining still unclear.

In spite of these intense studies outlined above, a deep understanding of phase separation in the SLR and its effect on subsequent crystallization has still not been achieved. In particular, we have little knowledge of the kinetic mechanism, microstructural evolution and dynamic features associated with the phase separation. In any case, it is hard to understand the incubation period during which phase separation occurred but no interference contrast was detected in the SANS experiment. Furthermore, from the thermodynamic point of view, structural relaxation in the SLR via phase separation should lead to formation of supercooled liquids exhibiting a higher thermal stability against crystallization, compared with the homogeneous amorphous state. Therefore, a systematic investigation of the dynamics and microstructural evolution during structural relaxation in the SLR is still required. As a powerful tool for studying phase transitions in condensed matter, SANS exhibits some advantages over the other techniques. Specifically, an *in-situ* SANS facility available in the BER-II reactor of Germany [26] makes the present study very attractive.

In this paper, we shall apply *in-situ* SANS to investigate the phase separation and crystallization in amorphous $Cu_{12.5}Ni_{10}Zr_{41}Ti_{14}Be_{22.5}$. We shall pay attention to the effect of phase separation on the subsequent crystallization, and also to the microstructural evolution and the kinetic and dynamic behaviours during the phase separation. By carefully processing the SANS data, we shall clear up some misunderstandings and present a relatively complete picture of the phase separation.

2. Experimental method

The bulk samples of amorphous $Cu_{12.5}Ni_{10}Zr_{41}Ti_{14}Be_{22.5}$ were prepared by remelting the solidified ingots with nominal constitution in sealed silica tubes containing pure Ar gas at a pressure greater than 1.0 atm and subsequently quenched into water. The amorphous state of the samples was confirmed by X-ray diffraction, TEM and SANS. The supercooled liquid state of this alloy, ranging from 620 to 671 K, was determined using DSC at a heating rate of 4 K min^{-1}, although this range may vary a little depending on the heating rate [17]. The disc-like samples of 10 mm diameter and 1.0 mm thickness were polished on both sides before use to avoid any surface effect on the scattering.

The *in-situ* SANS experiment was performed in the V4 instrument installed in the BER-II reactor at the Hahn-Meitner-Institut Berlin of Germany. For details of the instrumentation, we refer to [26]. Neutrons with a wavelength of 0.6 nm were used and the sample–detector distance varied between 1.21 and 16.00 m, with the moment transfer (the wavevector in the scattering geometry), q, covering the range from 0.03 to 2.00 nm^{-1}, considering the fact that the

scattering length density showed a scale from several nanometres to more than 10 nm. During measurements, the samples were individually placed into the furnace installed in the SANS spectrometer. The temperature of the sample can be precisely controlled to within ± 1 K over a sufficiently long time. The two-dimensional neutron detector consisting of 64×64 cells was cycled between the two assigned distances (here they were between 1.21 and 8.00 m) with an acquisition time of about 5 min at each position and with a moving time of 3 min in between the two positions. At several times during the *in-situ* detection, the detector was positioned at 16.00 m from the sample in order to probe the signals in the very-low-q range.

Each sample was annealed for 2 min at the nominal temperature after heating from the previous temperature. In our experiments, scattering signals from samples isothermally annealed in the range 600–700 K for different times were collected. After careful corrections for the background, transmission and efficiency of the detector, the scattering function, $S(q,t)$, at different temperatures and times was obtained. By reference to the scaling of a water standard intensity, $S(q,t)$ can be obtained on an absolute scale in reciprocal centimetres.

3. Experimental results

3.1. Scattering profiles

To gain an overall view of the structural relaxation and crystallization in the alloy, we first present our elementary observations of the scattering patterns. Fig. 1 gives a typical two-dimensional equal-intensity contour of the scattering from the alloy annealed in the SLR. It is clearly shown that the scattering was perfectly isotropic. Based on this fact, all data to be presented below was processed by a radial average of the scattering profile and q is then referred to as the radial wavevector.

Fig. 2 presents the scattering functions for samples annealed at several temperatures and for different times, on a log–log scale. Clearly, all the curves except that for $T = 673$ K did exhibit a distinct peak pattern and revealed phase separation events, although large differences in both the peak intensity and the shape of these curves from one to another were displayed. A strong temperature dependence of the scattering was revealed. An increase in the scattering peak of about ten times was observed as the annealing temperature rose about 20 K. In spite of the fact that $T_g \approx 620$ K, the sample annealed at $T = 613$ K for a sufficiently long time (120 h) had already relaxed via phase separation. No crystallization feature from the sample annealed at 650 K for 3 h was detected. Nevertheless, as the temperature increased to 673 K (T_x of the alloy), crystallization started after a short time, and in contrast no phase separation was identified.

3.2. In-situ observations

To observe structural evolution of the alloy annealed to 673 K, *in-situ* measurement was carried out and the

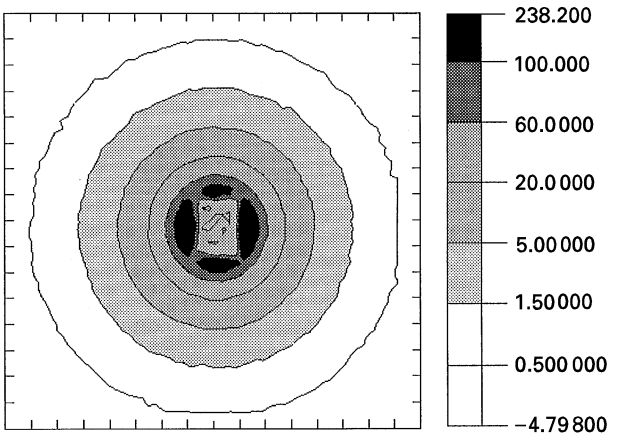

Figure 1 The two-dimensional pattern of SANS from amorphous $Cu_{12.5}Ni_{10}Zr_{41}Ti_{14}Be_{22.5}$ alloy annealed in the supercooled liquid range. The detector consists of 64×64 cells.

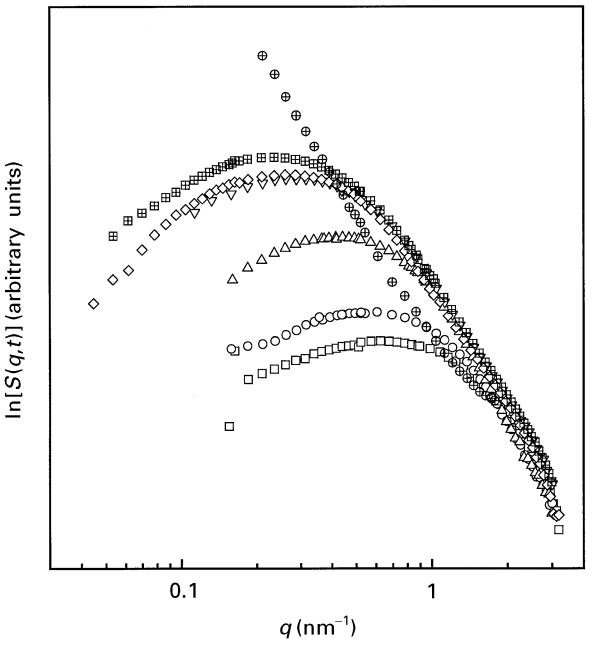

Figure 2 The scattering functions for amorphous $Cu_{12.5}Ni_{10}Zr_{41}Ti_{14}Be_{22.5}$ annealed at several temperatures for different times. (□), 613 K, 120 h; (○), 616 K, 10 h; (△), 623 K, 10 h; (▽), 633 K, 15 h; (◇), 640 K, 12 h; (■), 650 K, 3 h; (⊕), 673 K, 0.2 h.

data are presented in Fig. 3, also on a log–log scale. For convenience, this sample is called sample I. At $t = 0$, very weak and almost constant $S(q,t)$ was achieved over the total range q. This obviously arose because of the Laue and incoherent scattering contributions, indicating the absence of large-scale inhomogeneity and crystalline phase. However, in the initial 10 min of annealing, the scattering function acquired rapid growth. The lower q, the faster $S(q,t)$ grew. No peak pattern was distinguished. Up to about 30 min, the scattering reached an almost saturated state. Subsequently an identifiable change in $S(q,t)$ occurred only for two events of sufficiently long gap. Here it is interesting to note that after about 10 min the scattering function can be fitted quite well to the Porod law, as shown by the broken line in Fig. 3, where deviation of the data from the line in the high-q range was attributed to the background noises.

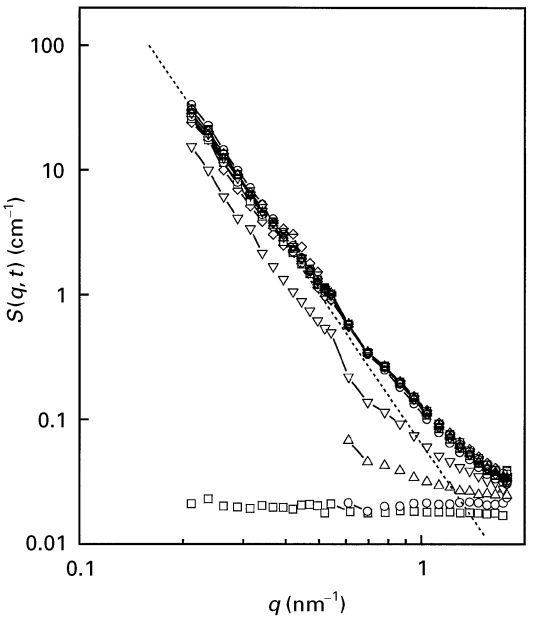

Figure 3 The time evolution of the scattering function for amorphous $Cu_{12.5}Ni_{10}Zr_{41}Ti_{14}Be_{22.5}$ (sample I) annealed at $T = 673$ K for various times. (□), 0 min; (○), 3 min; (△), 6 min; (▽), 10 min; (◇), 73 min; (⊡), 130 min; (⊙), 200 min; (△), 340 min; (▽), 380 min; (◈), 520 min; (⊟), 640 min; (⊖), 720 min.

Therefore, on direct heating from room temperature to 673 K, the alloy immediately started to crystallize and no phase separation was observed before and during crystallization.

Furthermore, it can be assessed that crystallization of the alloy at 673 K was quite limited since the scattering followed the Porod law [27]. Our estimation shows that the interparticle spacing of the crystals must be larger than 60 nm. The TEM observations confirmed that volume fraction of the crystalline phase was only 1.0%. Therefore these crystals were several nanometres in size.

As shown in Fig. 2, phase separation in all samples annealed in the SLR was detected. To obtain a deep insight into the sequence and its effect on subsequent crystallization, we annealed two samples at $T = 620$ K and 643 K respectively, for a sufficiently long time; we then increased their temperature to $T = 673$ K and again annealed them for a very long time. These samples are called samples II and III, respectively. During these anneals, *in-situ* measurement of the scattering was carried out. The results are presented in Figs 4 and 5, respectively. In Figs 4a and 5a, the time evolutions of the scattering functions for samples II and III annealed at $T = 620$ K and 643 K, respectively, are plotted. The part between zero and the cut-off of the low-q range for each curve may be artificially connected with the broken lines, as presented in Fig. 5a. This artificial connection was confirmed by our measurement of the scattering in the very-low q range for each sample. In Fig. 6a is plotted the scattering for sample II annealed at $T = 620$ K and 1200 min. It is clearly shown that $S(q, t)$ decayed rapidly even when q decreased to 0.035 nm^{-1} (the corresponding real-space length was 180 nm), predicting that no crystallization was involved in the sample and the products of the process were still supercooled

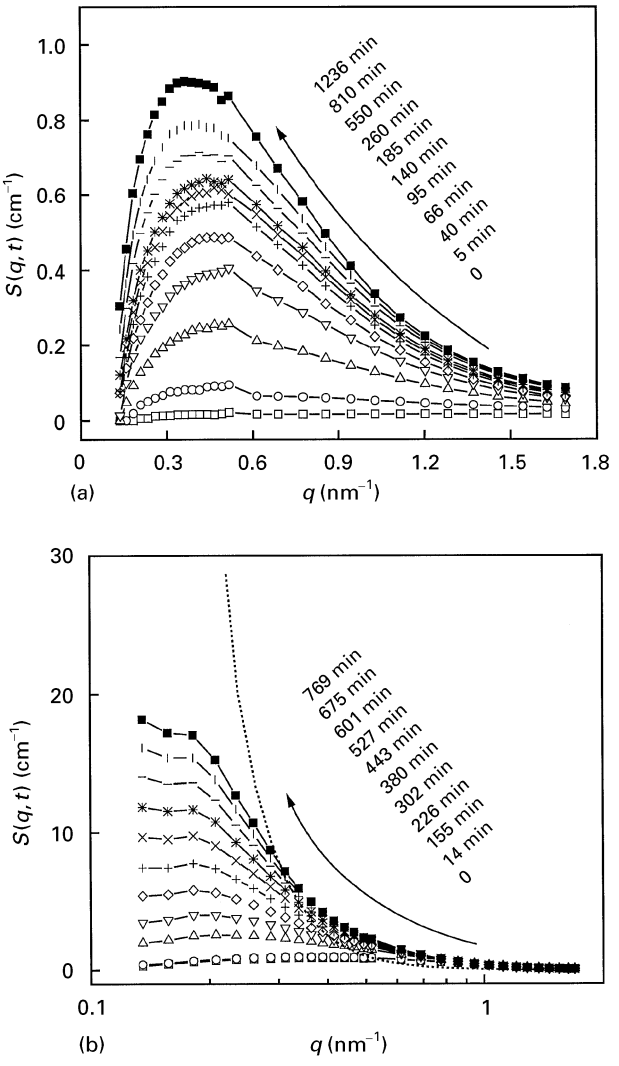

Figure 4 The time evolution of the scattering function for amorphous $Cu_{12.5}Ni_{10}Zr_{41}Ti_{14}Be_{22.5}$ (sample II) (a) annealed at $T = 620$ K for the indicated times and (b) then annealed at $T = 673$ K for the indicated times. The arrows indicate time flows. The broken line in (b) represents the scattering from the alloy annealed at $T = 673$ K for about 30 min.

liquids. The TEM observations of a similar sample showed weak alternative contrast variation and diffusive diffraction rings but no distinct spot. Figs 4b and 5b show time evolution of the scattering function for samples II and III, respectively, at $T = 673$ K. The dashed lines represent the scattering from sample I annealed at $T = 673$ K for 30 min.

First, let us look at the scatterings in the SLR. As shown in Figs 4a and 5a, the scattering patterns indicated propagation of typical phase separation in the samples. At both temperatures, we observed a rapid increase and peak shift in the scattering spectrum immediately after the annealing began. The phase separation proceeded quite quickly in the early stage but significantly decelerated with time, until the late stage where an identifiable change in $S(q, t)$ was acquired only by comparing two events with a sufficiently long time gap.

Considering the scattering in the low-q range, it increased as a power function of q with an exponent of about 3.0, but lower in the earlier stage. This exponent is a little less than the value of 4.0 normally achieved

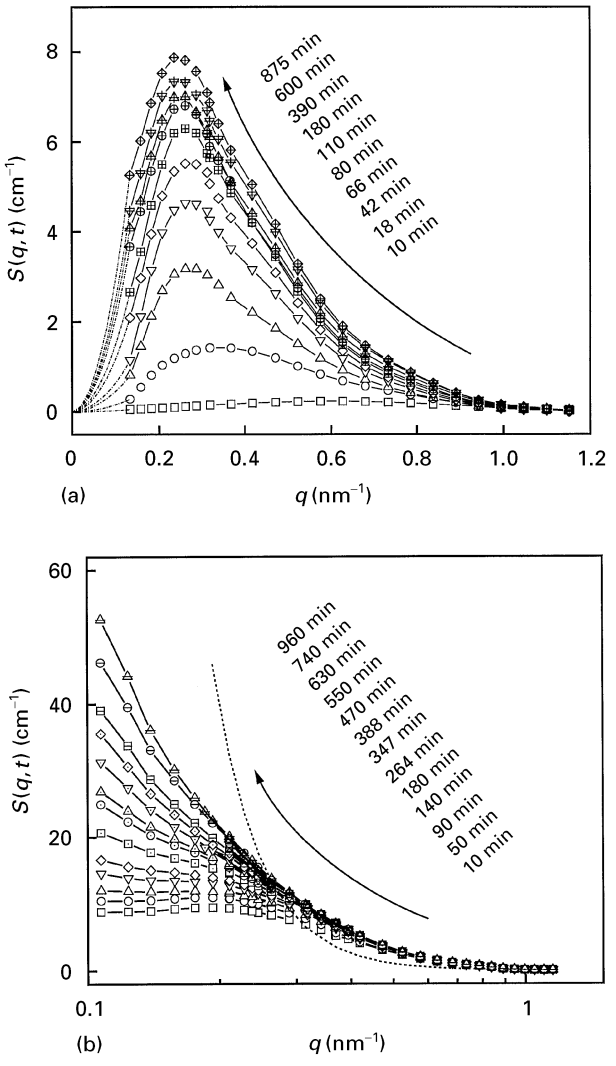

Figure 5 The time evolution of the scattering function for amorphous $Cu_{12.5}Ni_{10}Zr_{41}Ti_{14}Be_{22.5}$ (sample III) (a) annealed at $T = 643$ K for the indicated times and (b) then annealed at $T = 673$ K for the indicated times. The arrows indicate time flows. The broken line in (b) represents the scattering from the alloy annealed at $T = 673$ K for about 30 min.

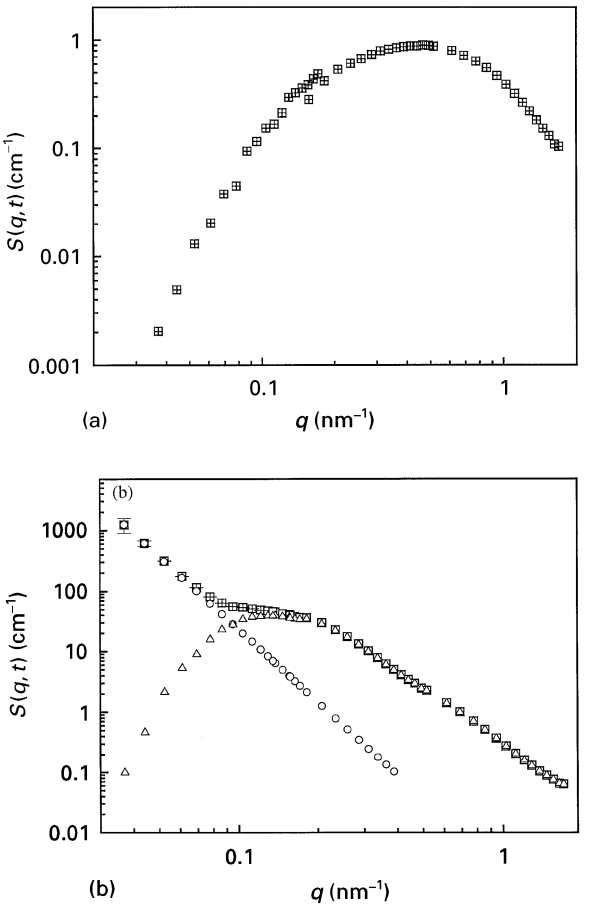

Figure 6 The scattering spectrum for amorphous $Cu_{12.5}Ni_{10}Zr_{41}Ti_{14}Be_{22.5}$ (sample II) (a) annealed at $T = 620$ K for 1200 min and (b) then at $T = 673$ K for 1200 min. (□), scattering function $S(q, t)$; (○), best fit of the low-q tail of $S(q, t)$, i.e., $S_C(q, t)$; (△), between differences, $S(q, t)$ and $S_C(q, t)$, i.e., $S_D(q, t)$ (see text).

for the nucleation even with a very low volume fraction of precipitates [28, 29]. However, for the scattering in the high-q range, all samples (see also Fig. 2) showed that the decay of the scattering can be roughly fitted to the Porod law. This means that a finite Porod constant, K, exists;

$$K(t) = \lim_{q \to \infty} [q^4 S(q, t)] \tag{1}$$

which, of course, increased with time. This predicted that the scattering arose because of the interference of isolated droplets embedded in the matrix. As shown in Fig. 6a, because there was no crystallization in the samples, it is argued that both the droplets and the matrix were still supercooled liquids. They might have different compositions but were not significantly different in their atomic arrangements. This argument is supported by the APFIM measurements of the samples which probed anticorrelated fluctuations of at least Ti and Be but did not develop the image showing grain-boundary structure. Another argument from good fitting of the high-q-range decay by the Porod law is that the droplet-like liquid occupied only a low volume fraction.

As the temperatures of samples II and III which were previously annealed in the SLR for a sufficiently long time were increased to 673 K, the crystallization point of the alloy, we observed quite different scattering spectra from those shown in Fig. 3. As plotted in Figs 4b and 5b, for both samples, after the increase we observed rapid increase in the scattering, not only in the scattering peak but also especially in the low-q part which increased much more rapidly than the other parts. Up to about 700 min the peak or convex pattern of the scattering profile in Fig. 4b could be identified; the scattering after about 140 min in Fig. 5b no longer exhibited a single-peak pattern. These phenomena were, of course, attributed to crystallization in the samples. Nevertheless, it is interesting to note that the scattering spectrum at any time reflected by samples II and III showed considerable deviations from the sequences in sample I. No Porod behaviour of the scattering function was observed. In particular, the intensity in the low-q range after a sufficiently long anneal was still much lower than that achieved by sample I annealed only for 30 min, as shown by the dashed lines in Figs 4b and 5b. These results suggest firstly that, as annealed at $T = 673$ K, samples II and III also acquired a crystalline phase, similar to sample I, but much less in volume than that formed in sample

I and secondly and more markedly that further structural relaxation, which was no doubt the consequence of the previous events in the SLR, might be initiated. This argument again has support from the TEM observations where the coexistence of separated spots and diffusive rings in the diffraction pattern was revealed. The microstructures of samples II and III consist of small crystals embedded in the phase-separated disordered matrix, whereas sample I acquired small crystals embedded in homogeneous amorphous matrix.

3.3. Separation of the sequences at $T = 673$ K

As we argued, both crystallization and phase separation occurred in samples II and III as annealed at $T = 673$ K. To obtain a deep understanding of the processes, it is necessary to separate the contributions from the crystals and phase-separated supercooled liquid to the scattering spectrum. Let us look at the scattering spectrum from sample II annealed at 673 K for 1200 min, as shown in Fig. 6b. The open squares represent $S(q, t)$ which can be written as

$$S(q, t) = S_C(q, t) + S_D(q, t) \quad (2)$$

where S represents the scattering function, and the subscripts C and D refer to crystallization and decomposition, respectively. Although large errors were included in the very-low-q part of $S(q, t)$, however, if we ignore the errors, the intensity in this range can be roughly fitted to the Porod law. Note the fact that the interference of the very-low-q range from a phase separation sequence could be ignored as a good approximation. We can conclude that the scattering from these isolated crystals definitely followed the Porod law for the overall q range investigated here, because sample I reflected neutrons exactly according to this law, as shown in Fig. 3.

Starting from this point, we separated this scattering profile into two parts, as shown in Fig. 6b, where the open circles represent the fit of the very-low-q tail by the Porod law, i.e., the scattering from the crystals, $S_C(q, t)$, and the open triangles represent the difference between $S(q, t)$ and $S_C(q, t)$, i.e., that from the inhomogeneity due to phase separation, $S_D(q, t)$. It should be pointed out that this processing would contain considerable errors for the very-low-q tail of $S_D(q, t)$, but the other data must be sufficiently accurate as $S_C(q, t) \propto q^{-4}$. With this procedure, we separated successfully all the data shown in Figs 4b and 5b into two parts; the part $S_D(q, t)$ is presented in Fig. 7a and b, respectively. From Fig. 7, we can conclude that, in parallel to the crystallization, a further phase separation in samples II and III is initiated after the temperature increase to 673 K. Compared with the sequence in the SLR, the new phase separation exhibited a faster coarsening stage, and again it has been found that the high-q tail of the scattering functions decayed according to the Porod law.

We have presented all experimental data that we obtained. In the following sections, we shall turn to the further analysis of the data and give a detailed description of the effect of structural relaxation in the SLR on the subsequent crystallization, kinetic mechanism and dynamics of the phase separation and microstructural evolution.

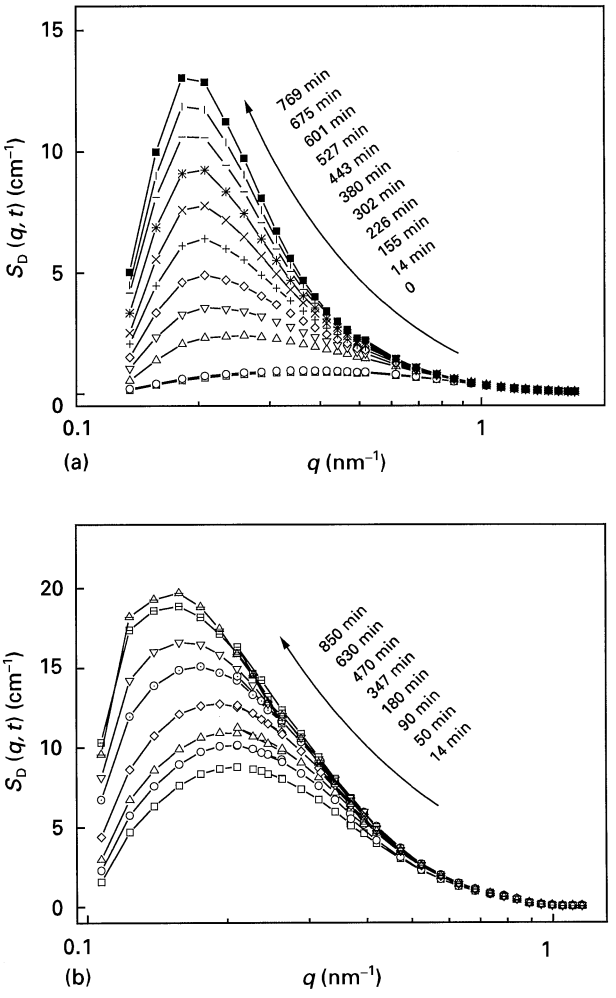

Figure 7 The time evolution of the scattering function $S_D(q, t)$ for amorphous $Cu_{12.5}Ni_{10}Zr_{41}Ti_{14}Be_{22.5}$ annealed at $T = 673$ K for the indicated times after the alloy was previously relaxed (a) at $T = 620$ K for 1200 min (sample II) and (b) at $T = 643$ K for 880 min (sample III). The arrows indicate time flows.

4. Effect of phase separation on crystallization

As we mentioned in the introduction, Schneider *et al.* [18] argued from their observations that phase separation in the SLR in fact destabilized the amorphous state, since nanocrystals precipitated from the amorphous matrix was already observed in the SLR. Our observations of similar samples under the same conditions did not identify may crystalline particles, as shown in Fig. 6a. Furthermore, because we obtained the scattering spectra from the crystalline particles at different times for samples I–III, it is possible to study quantitatively the effect of the structural relaxation in the SLR on the subsequent crystallization around T_x.

Fig. 8a gives the Porod constant, K, of the crystallization sequences in samples I–III at $T = 673$ K as a function of time. It is quite clear that crystallization in sample I nearly ceased after rapidly developing in the initial tens of minutes, however, samples II and III

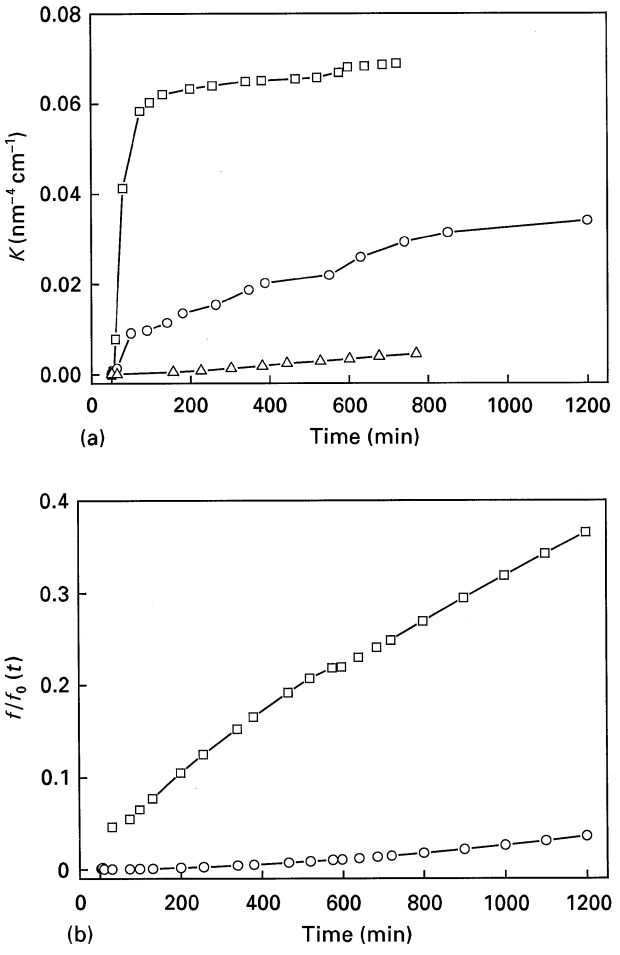

Figure 8 (a) The evaluated Porod constant K of the scattering from the crystalline phase in amorphous $Cu_{12.5}Ni_{10}Zr_{41}Ti_{14}Be_{22.5}$ annealed at $T = 673$ K. (□), sample I; (△), sample II; (○), sample III; (b) The time dependence of the volume fraction of crystallined phase formed in sample II (○) and sample III (□) annealed at $T = 673$ K, with respect to that achieved in sample I annealed at $T = 673$ K.

exhibited a gradual increase in crystallization and a much smaller K than for sample I.

It is reasonable to assume that the crystalline particles in the samples had a sharp interface with the matrix. Therefore, the interfacial area of the particles per unit volume can be obtained [30]:

$$\Omega_C(t) = \frac{K(t)}{2\pi\,\Delta\eta^2} \tag{3}$$

with $\Delta\eta$ representing the contrast factor [27]:

$$\Delta\eta = \left(\sum_i c_i b_i \rho_i\right)_M - \left(\sum_i c_i b_i \rho_i\right)_P \tag{4}$$

where c_i, b_i and ρ_i are the atomic concentration, scattering length and atomic density of species i; the subscripts M and P denote the matrix and precipitate (here the crystalline phase). Because $\Delta\eta$ is constant as soon as the crystalline particles formed, we can easily derive the ratio of the volume fractions of the crystalline phase for any two samples 1 and 2 to be considered:

$$\frac{f_1}{f_2} = \left(\frac{K(1,t)}{K(2,t)}\right)^{3/2} \tag{5}$$

where f is the volume fraction, and the numbers 1 and 2 refer to samples 1 and 2. Assuming that the volume fraction in sample I is f_0, we get the volume fraction in samples II and III with respect to f_0 as a function of time of annealing at $T = 673$ K, as shown in Fig. 8b. This indicates that the crystalline phase formed in samples II and III as annealed at 673 K was always less than that formed in sample I annealed for the same time, although the ratio between them increased with time and strongly depended on the temperature of the phase separation in the SLR. In particular, sample II annealed for 1200 min acquired such a small amount of crystalline phase that it was only 3–4% of that achieved in sample I. A rough estimation showed that the amount of the crystalline phase in sample I annealed at 673 K only for 30 min equalled that in samples II and III annealed at 673 K for 24 000 min and 3000 min, respectively. This result gives direct evidence for the argument that the structural relaxation via phase separation in the SLR promotes the thermal stability of the alloy against crystallization. In other words, we believe that the products of the phase separation showed higher resistance to crystallization, compared with the initial amorphous state.

5. Microstructural evolution

5.1. Structural parameters

Now we look again at the microstructural evolution during the phase separation both in the SLR and around T_x. For sample II annealed at 620 K and then at 673 K, from Figs 4a and 7a, and for sample III annealed at 643 K and then at 673 K, from Figs 4b and 7b, we can evaluate a series of parameters of the phase-separating microstructure, as functions of time. First, we define the nth moment $S_D^2(t)$ and its normalized form $q_n(t)$ of the scattering function as

$$S_D^n(t) = \int_0^{q_H} q^n\, S(q,t)\,\mathrm{d}q + \int_{q_H}^{\infty} K(t)\, q^{n-4}\,\mathrm{d}q \quad n = 0, 1, 2$$

$$q_n(t) = \frac{S_D^n(t)}{S_D^0(t)} \quad n = 1, 2 \tag{6}$$

where q_H is the high-q cut-off of the scattering curve. Obviously, the first-order moment q_1 scales the characteristic length of the phase-separating microstructure. $S_D^2(t)$ is in fact the invariant of the scattering, which can be formulated for the case of isolated particle precipitating from the matrix [30]:

$$S_D^2(t) = 2\pi^2\,\Delta\eta^2\,\phi(1-\phi) \tag{7}$$

with ϕ denoting the volume fraction of the precipitates and $\Delta\eta$ again for the contrast factor between the particles and matrix. Furthermore, we found there exists a well-behaved Guinier zone of all the scattering functions achieved here, just on the right-hand side of the peak, as plotted according to the Guinier approximation [30]:

$$S(q,t) = S_0 \exp\left(-\frac{R_g^2 q^2}{3}\right) \tag{8}$$

where S_0 is a positive constant and R_g is the well-known radius of gyration which scales the average size of the isolated precipitates.

The evaluated $q_1(t)$, $R_g(t)$ and $S_D^2(t)$ of the phase-separating structure, as functions of time, are presented in Fig. 9a, b and c, respectively. Here the arrows indicate the time at which the sample temperature was increased from the SLR (620 K for sample II and 643 K for sample III) to 673 K. First, let us look at the sequences in the SLR (left-hand sides of the arrows). For both samples, rapid increase in $S_D^2(t)$ and $R_g(t)$ and a decrease in $q_1(t)$ were achieved in the early stage; subsequently we observed a considerable slowing-down of these changes, until a late stage where the microstructure showed indiscernible change; in spite of this the change in $S_D^2(t)$ was relatively stronger. This predicted that composition modulation and precipitation of the droplets should be completed in the rapidly changing time scale, followed by coarsening of the microstructure as the dominant process. The characteristic length of the microstructure, $2\pi/q_1$, was much larger than $R_g(t)$, supporting the argument that one product of the phase separation was droplet-like but not inter-connected supercooled liquid, embedded in the matrix of the other product.

When the samples were heated to 673 K after a sufficiently long-time relaxation in the SLR, we observed a significant jump in and then a strong evolution of these parameters. The droplet size acquired marked growth; meanwhile the interspacing increased. Even after several hundreds of minutes, the process went ahead at a considerable rate, although the slowing-down effect was also obvious, exhibiting different features from those in the SLR. It should be pointed out here that a similar change in $S_D^2(t)$ to those in $q_1(t)$ and $R_g(t)$ after the temperature increase suggested that not only did the microstructure coarsening propagate as a response to the temperature fluctuation, but also a new phase separation occurred, as argued earlier.

It was again demonstrated that the microstructure formed in the SLR depended significantly on temperature. Even after annealing both sample II and sample III at 673 K, the microstructure difference between them was still marked. Nevertheless, in spite of the fact that no data at a very long time were obtained, from Fig. 9 it was observed that the microstructures of both samples tended to evolve in the same way and, in particular, the parameter $S_D^2(t)$ of both samples had already coincided after annealing for about 400 min.

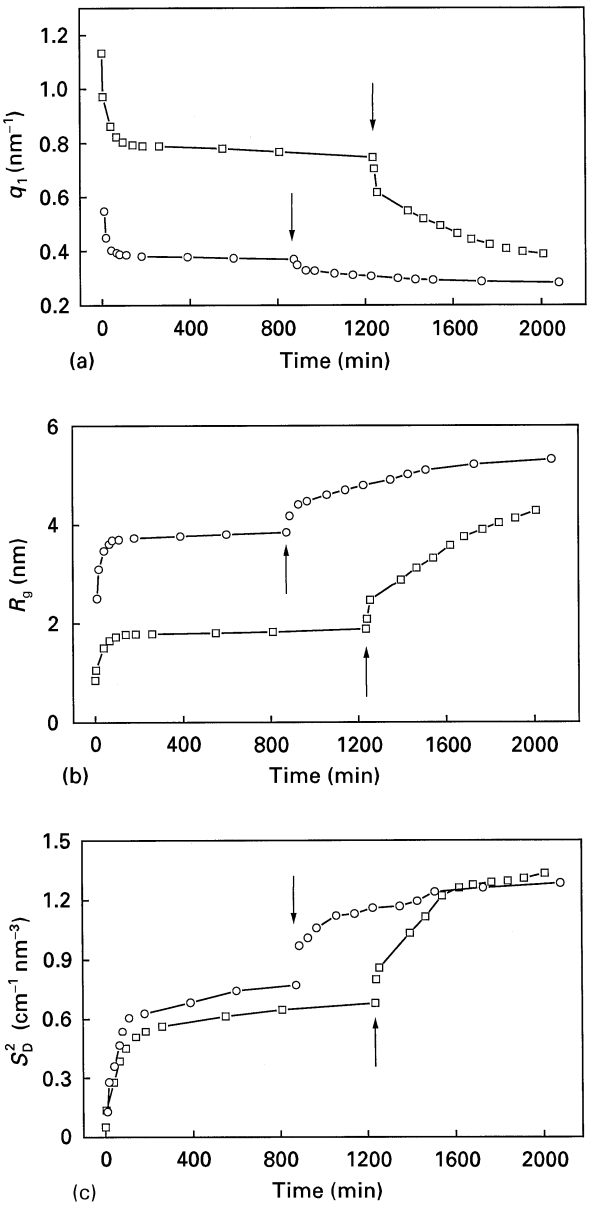

Figure 9 The structural parameters of phase-separating microstructure, (a) q_1, (b) R_g and (c) S_D^2 plotted against time for amorphous $Cu_{12.5}Ni_{10}Zr_{41}Ti_{14}Be_{22.5}$ annealed at $T = 620$ K and then at $T = 673$ K (sample II) (□), and at $T = 643$ K and then $T = 673$ K (sample III) (○), The arrows indicate the times at which the temperature changed.

5.2. Correlation function

The microstructural evolution during phase separations can also be clearly illustrated by evaluating the correlation function, $g(r, t)$ [30]:

$$g(r, t) = \frac{1}{2\pi^2} \int_0^\infty \frac{\sin(qr)}{qr} S(q, t) q^2 \, dq \qquad (9)$$

where r represents the separation between two correlating points. Because the low-q cut-off induces only a negligible error in $g(r, t)$, Equation 9 can be rewritten as

$$g(r, t) = \frac{1}{2\pi^2} \left(\int_{q_L}^{q_H} \frac{\sin(qr)}{qr} S(q, t) q^2 \, dq + \int_{q_H}^{\infty} \frac{\sin(qr)}{qr} \frac{K(t)}{q^2} \, dq \right) \qquad (10)$$

where q_L is the low-q cut-off of the measured scattering. As an example, the calculated $g(r, t)$ for sample II annealed in the SLR are plotted in Fig. 10. Similar profiles for other sequences both in the SLR and at 673 K were obtained. Fig. 10a gives the overall profiles of $g(r, t)$ at several times, from which we have shown that, against r standing from zero, each of the curves decayed rapidly and passed through the first zero point and then exhibited indiscernible oscillation

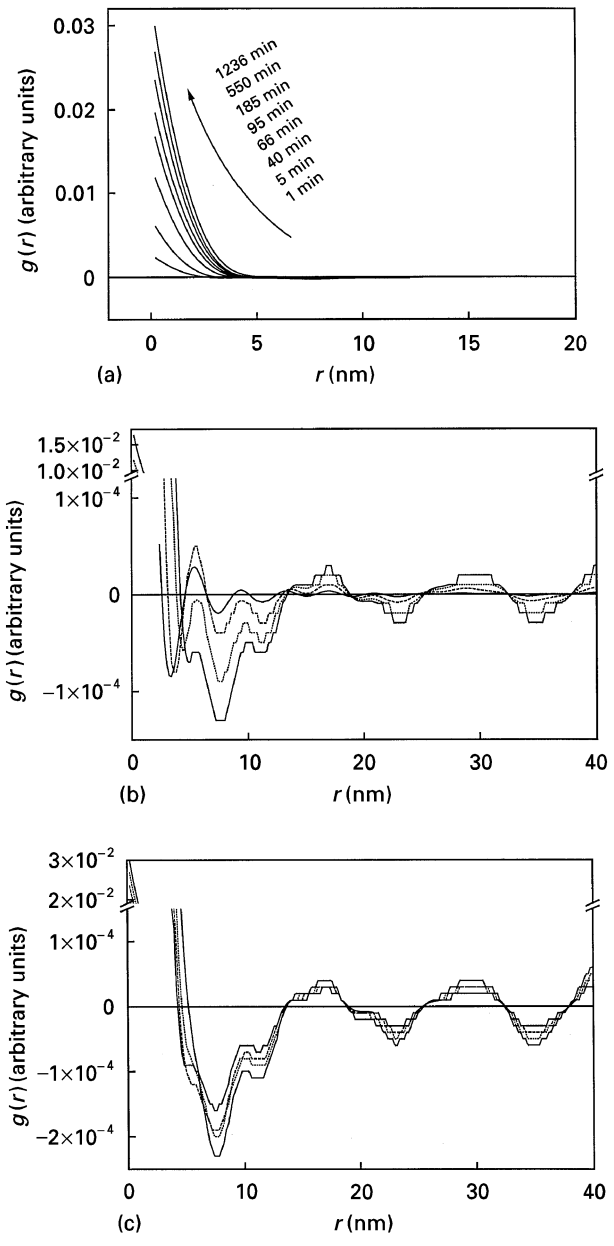

Figure 10 (a) The correlation functions $g(r, t)$ for the phase separation at $T = 620$ K in amorphous $Cu_{12.5}Ni_{10}Zr_{41}Ti_{14}Be_{22.5}$ (sample II). The arrow indicates time flow. (b) $g(r, t)$ at 1 min (——), 5 min (------), 40 min (·····) and 66 min (——). (c) $g(r, t)$ at 95 min (——), 185 min (------), 550 min (·····) and 1236 min (——).

around $g(r, t) = 0$. The left-hand part of the first zero point increased with time. These curves show a typical profile of a two-phase system with one minor droplet-like phase embedded in the matrix of the other major phase. Furthermore, as we refer to the fine structure of these curves on the right-hand side of the first zero point, as shown in Fig. 10b and c, details of the evolution of $g(r, t)$ have been revealed. We have observed a strong evolution of $g(r, t)$ in the early stage, characterized by a tremendous increase in both the wavelength and the amplitude of the oscillation. Towards the late stage, significant slowing-down of the change was observed. Because the first and second zero points of $g(r, t)$ scale with the average size and interspacing of the droplets, respectively, strong modulation and coarsening of the microstructure in the early stage were obvious.

It is interesting to note the relatively regular oscillation $g(r, t)$ on the right-hand side of the first minimum achieved after annealing for only about 60 min. An almost constant pattern and no decay in the oscillation as functions of r were observed. This predicts that, towards the late stage, these droplets are distributed regularly in the matrix with a narrow size distribution. Meanwhile, we found that the oscillation periodicity was roughly consistent with the scale represented by $2\pi/q_1$, confirming $q_1(t)$ as a relatively precise scale of wavelength of the microstructural modulation.

5.3. A simple approach

In this section, we propose a simple approach to the density, size and volume fraction of the droplets as functions of annealing time. From the last section we understand that the droplet-like phase is distributed regularly and $q_1(t)$ scaled well with the modulation wavelength. As quite a good approximation, the droplet density in the microstructure is given by N_p:

$$N_p = \left(\frac{q_1}{2\pi}\right)^3 \tag{11}$$

The average volume of each droplet, V_p, and the volume fraction of the droplets, ϕ, can be given as:

$$V_p = \frac{4\pi\theta R_g^3}{3}$$
$$\phi = N_p V_p \tag{12}$$

where θ is a factor for shape correction and equals $(\frac{5}{3})^{3/2}$ for the sphere-like pattern. Choice of this factor does not induce considerable error for an estimation of the droplet volume. The evaluated N_p, V_p and ϕ for both sample II and sample III, based on this approach, are plotted in Fig. 11a, b and c, respectively. The arrows again indicate the time for temperature increase. While it is reasonable that both N_p and V_p showed the same behaviours as q_1 and R_g, it is a little surprising to find that ϕ did not show a strong temperature dependence and no longer changed after a rapid increase in the very early stage of annealing in the SLR. After heating to 673 K, sample II acquired a more droplet-like phase and then ϕ increased from about 10% to 16%, whereas in sample III there was nearly no change in ϕ.

An important fact revealed here is that N_p for all cases exhibited a monotonic decrease from the beginning, which predicts that the mechanism for each phase separation sequence may not be nucleation and growth, unless the nucleation had been completed before the earliest event detectable. Otherwise, we should observe a single-peak convex pattern of N_p as a function of time. More evidence for this prediction will be given below. On the other hand, an estimate from th APFIM probed spectra of the composition fluctuation [18] gave $\phi \approx 18\%$. A best fit of the scattering function by the Fratzl–Lebowitz [31] equation [32] yielded $\phi \approx 6$–8%. These values are not very different from our evaluation and provide support for our simple approach.

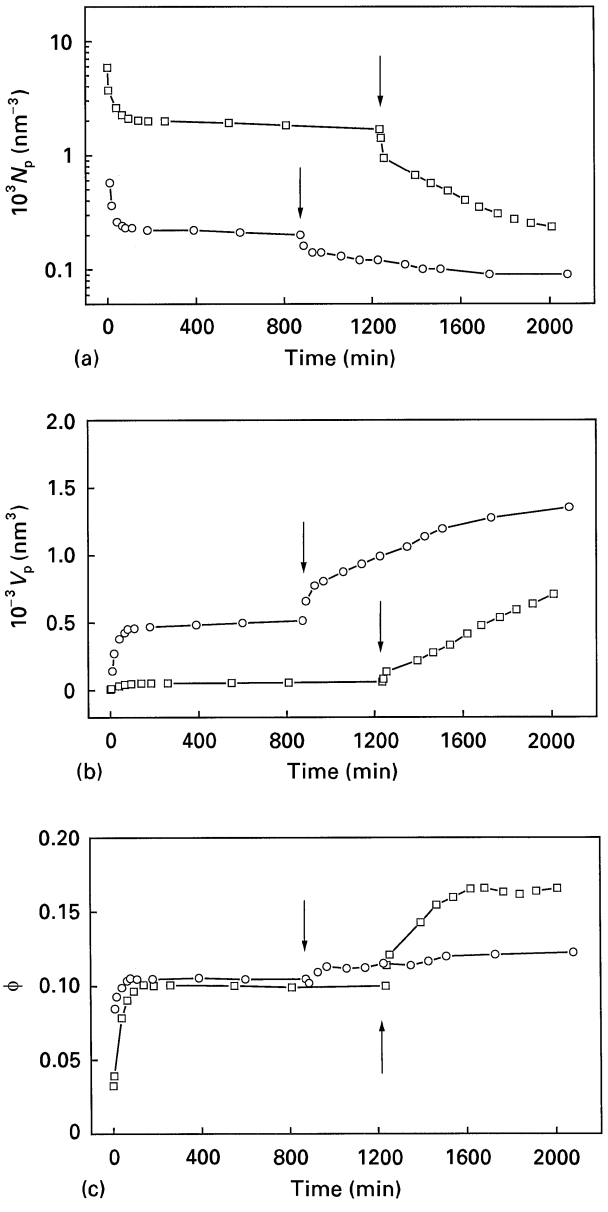

Figure 11 The structural parameters of phase-separating microstructure, (a) N_p, (b) V_p and (c) ϕ, plotted against time for amorphous $Cu_{12.5}Ni_{10}Zr_{41}Ti_{14}Be_{22.5}$ annealed at $T = 620$ K and then at $T = 673$ K (sample II) (□), and at $T = 643$ K and then $T = 673$ K (sample III) (○), The arrows indicate the times at which the temperature changed.

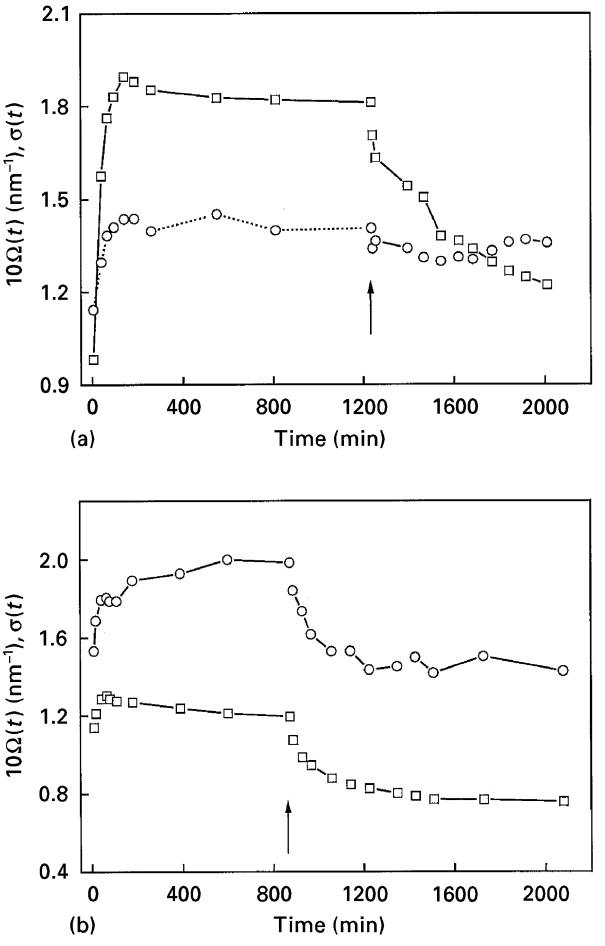

Figure 12 The time dependence of the sharp interfacial area, Ω_D, between the droplet-like supercooled liquid and matrix per unit volume (□) and the shape factors, σ, of these droplets, (○) for the phase-separating microstructure of amorphous $Cu_{12.5}Ni_{10}Zr_{41}Ti_{14}Be_{22.5}$ annealed (a) at $T = 620$ K and then at $T = 673$ K and (b) at $T = 643$ K and then $T = 673$ K. The arrows indicate the times at which the temperature changed.

5.4 Interfacial area and morphology of droplets

Applying the Porod limit, we can develop a parameter which scales with the droplet shape, characterized by its deviation from the isotropic pattern (sphere). By substituting Equation 7 into Equation 3, we get the sharp interfacial area, Ω_D, between the droplets and matrix, per unit volume of the sample [30]:

$$\Omega_D(t) = \pi\phi(1-\phi)\frac{K(t)}{S_D^2(t)} \tag{13}$$

From Equations 11 and 13 we obtain immediately the shape factor, σ, of the droplets with respect to a sphere of the same volume

$$\sigma(t) = \frac{\Omega_D(t)}{N_p(t)4\pi\frac{5}{3}R_g(t)^2} \tag{14}$$

which scales with the ratio of the interfacial area of a droplet to that of a sphere with the same volume.

The calculated $\Omega_D(t)$ and $\sigma(t)$ for both sample II and sample III, annealed both in the SLR and then at 673 K, are presented in Fig. 12a and b, respectively. Here we are especially interested in behaviours of $\Omega_D(t)$ in the SLR. At both temperatures, we observed a rapid increase in the initial stage (until about 100 min) and then a slow decay. The behaviour in the early stage again cannot be explained by the nucleation mechanism, which would result in a high value of $\Omega_D(t)$ in the early stage. During the decay period, coarsening was involved. After the temperature increased to 673 K, a rapid decrease in $\Omega_D(t)$ was attributed to further coarsening of the microstructure, whose kinetics were greatly temperature sensitive.

With respect to the shape factor in the SLR, we found that $\sigma \approx 1.4$–1.5 at $T = 620$ K and 1.9–2.0 at 643 K, ignoring the start-time data. Both were much larger than 1.0, indicating that the droplets deviated from the spherical shape. An estimate according to the ellipsoid pattern predicted that the ratio a/b, of the two half-axes, was 2.8 at 620 K and 6.0 at 643 K. This shaped droplet looked like a bar rather than an ellipsoid and acquired anisotropic morphology, especially

at higher temperatures. As the temperature changed to 673 K, the factor decreased a little, depending on the temperature at which the sample previously relaxed. In particular, for sample III, the decrease was marked. However, note that the droplets during this period were very large, up to 10 nm in size, which also contributed to the decrease in σ. Towards the late stage at 673 K, the factors for the two samples became comparable with each other.

6. Kinetics of phase separation

6.1. Mechanism of phase separation

To distinguish the mechanism dominating the phase separation sequence, the most direct evidence may be the contrast factor, $\Delta\eta$, as a function of time. It can be obtained from Equation 7, if $S_D^2(t)$ and $\phi(t)$ are known. In Fig. 13a is plotted the calculated $\Delta\eta^2$ against time for samples II and III, with the arrows indicating the times at which the temperature increased. It is quite clearly shown that for all cases the contrast factor increased gradually and not abruptly with time and then there was nearly no change. This gradually changing period was about 200 min at 620 K and about 100 min at 643 K. The relation between the contrast factor and $\Delta\eta_0$, the so-called "effective contrast factor", can be written as [27]

$$(\Delta\eta^2)^{1/2} \propto \frac{|\Delta\eta_0|}{1-\phi} \tag{15a}$$

with $\Delta\eta_0$ being defined as the difference in scattering contrast between the droplets and the homogeneous microstructure before phase separation:

$$\Delta\eta_0 = \left(\sum_i c_i b_i \rho_i\right)_{M_0} - \left(\sum_i c_i b_i \rho_i\right)_P \tag{15b}$$

where the subscripts M_0 and P denote the homogeneous alloy before decomposition and the droplets formed during decomposition, respectively. Because ϕ was very low, $|\Delta\eta_0|$ as a function of time behaved like $(\Delta\eta^2)^{1/2}$. This result convincingly demonstrated that the phase separation propagated via the spinodal mode, the dominant character of which is that the composition of the droplets fluctuates with time via a gradual mode. Referring to the nucleation mode, we would observe a roughly constant $\Delta\eta^2$ as soon as the first event of phase separation was detected.

The spinodal mode argument was supported by the monotonic decrease in $N_p(t)$ with time, as shown in Fig. 11a, and also by the increase in $\Omega_D(t)$ in the early stage, as shown in Fig. 12. From the latter evidence, we understand that, in the early stage of spinodal process, the interface between the droplets and matrix was not sharp, assuming that this interface can be defined.

Furthermore, the gradual increase in $\Delta\eta^2$ after the times indicated by the arrows in Fig. 13a showed that new phase separation occurred and a new droplet-like phase has formed once more in the matrix. However, it is unclear what the relation of these newly formed phases is with those formed previously in the SLR.

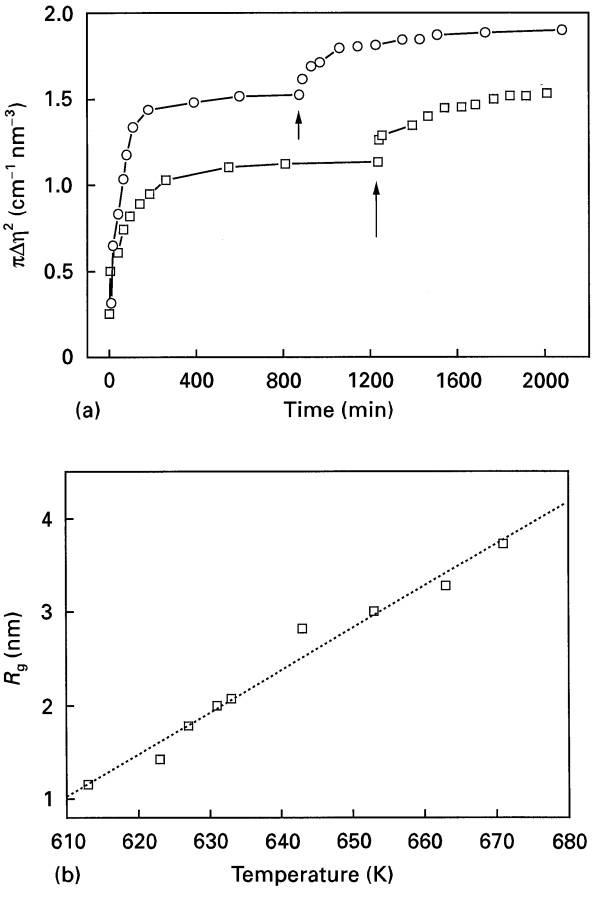

Figure 13 (a) The contrast factor, $\Delta\eta^2$, of the phase-separating microstructure plotted against time for amorphous $Cu_{12.5}Ni_{10}Zr_{41}Ti_{14}Be_{22.5}$ annealed at $T = 620$ K and then at $T = 673$ K (sample II) (□), and at $T = 643$ K and then $T = 673$ K (sample III) (○), The arrows indicate the times at which the temperature changed. (b) The radius R_g, of gyration, of the droplet-like supercooled liquid as a function of annealing temperature, in the alloy annealed for 10 h.

6.2. Temperature dependence

A temperature dependence of the kinetics of phase separation in the SLR was quantitatively derived, represented by a linear relation of R_g with temperature at a fixed time, as shown in Fig. 13b. The data represent the radius of gyration in samples annealed for 10 h at different temperatures, although there was a non-negligible error in the data from the linear dependence. This is a surprising result since we expected an exponential power when dealing with this dependence:

$$R_g \propto \exp\left(-\frac{aQ}{kT}\right) \quad a > 0 \tag{16}$$

where a is a positive constant, Q is the activation energy for diffusion and k is the Boltzmann constant. We argue that the linear dependence was at least partially attributable to the abnormal behaviour of the element diffusion, to be discussed below.

6.3. Kinetic exponent

For a phase-separating system, the late-stage kinetics would be a power function of time, i.e., the well-known Lifshitz–Slyozov–Wagner (LSW) law [33]. The

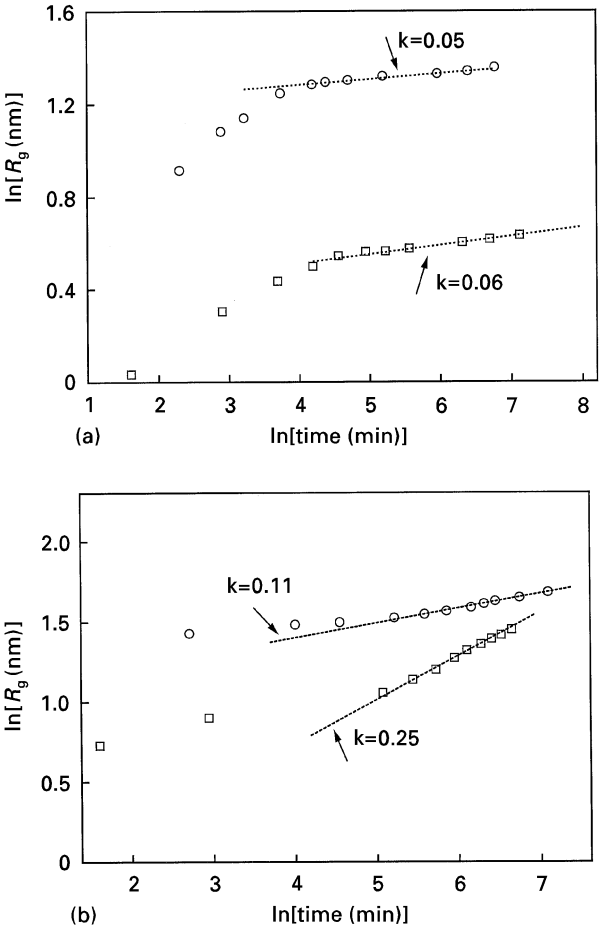

Figure 14 (a) The radius R_g, of gyration, plotted against time for amorphous $Cu_{12.5}Ni_{10}Zr_{41}Ti_{14}Be_{22.5}$ (a) annealed at $T = 620$ K (sample II) (□) and at $T = 643$ K (sample III) (○) and (b) then annealed at $T = 673$ K (for sample II) (□) and (sample III) (○). (----), the best fit of the data of the late stage by the power function of time.

well-proven value of this exponent is $\frac{1}{3}$, which characterizes the interfacial-energy-driven coarsening of the microstructure. In the present alloy, the data of $R_g(t)$ plotted against time are presented in Fig. 14, on a log–log scale, where Fig. 14a includes the data of the sequences for sample II at 620 K and sample III at 643 K, respectively, and the data for the samples annealed at 673 K after being fully relaxed in the SLR are given in Fig. 14b.

For the phase separation in the SLR, it seems that there roughly exist two time regimes which exhibit different kinetics and correspond to the so-called 'early stage' and 'late stage', respectively. In the early stage, the spinodal-type phase separation did not show a power dependence on time. In the late stage the microstructure coarsened and a power function of time was achieved, giving an exponent of 0.06 at 620 K and 0.05 at 643 K. Rather sluggish coarsening kinetics were achieved. It is well known that the elastic energy arising during the phase separation would prohibit coarsening; it must be quite weak here since we were dealing with a liquid system. We argue that such a small exponent is mainly attributed to the fact that in the present alloy the composition modulation imposed significant negative influence on the diffusitivity of some elements, such as Ni, Ti and Zr. The SIMS measurements of this alloy revealed that diffusion of some impurities, such as Co and Al, was considerably slowed during the phase separation in the SLR [25]. Let us look at the SLW equation:

$$R(t) \propto (D(t) d_0 t)^{k_0} \tag{17}$$

where R is the scale of the microstructure, $D(t)$ is the effective diffusivity of the elements, d_0 is the capillary length of the droplets and k_0 is the LSW exponent which equals $\frac{1}{3}$. As $D(t)$ decreased with time, the effective exponent k must become lower than k_0.

However, as the samples were reannealed at 673 K, the late-stage kinetics of the coarsening exhibited an exponent of 0.25 for sample II and 0.11 for sample III. They were higher than k observed in the SLR but still lower than $\frac{1}{3}$. Note here that there was crystallization in parallel to the new phase separation and the latter developed from the decomposed microstructure achieved in the SLR.

A small k value from phase separation has also been found for some previously investigated systems, such as Al–Si alloys ($k \approx 0.08$) [34] and Al–Zn–Mg alloys ($k \approx 0.08$) [35]. Our preferred explanation for such an anomalous behaviour in both alloys is the strong compositional and mechanical dependences of the diffusion of some elements, similar to the cases in the present system.

6.4. Size distribution

In this section, we obtain some information about size distribution of the droplet-like liquid in the matrix for the late stage. We present the data only for the SLR. In fact, the further phase separation of samples II and III at 673 K acquired a similar distribution in the final stage.

It is well recognized that the low-q part of the scattering function comes from the interference between droplets embedded in the matrix and that in the high-q range is attributed to the droplets themselves. As a good approximation, we formulate this function as [30]

$$S(q, t) = N P(q, t) H(q, t) \tag{18}$$

where N is the number of droplets in the irradiated zone of the sample, $P(q, t)$ is the form factor containing information on the size and shape of the droplets and $H(q, t)$ takes account of the interference effect in the microstructure. In the high-q range, $H(q, t)$ could be treated as a constant and $P(q, t)$ can then be obtained as

$$P(q, t) \propto \int \rho(R_0, t) \left(3 \frac{\sin(qR_0) - qR_0 \cos(qR_0)}{(qR_0)^3} \right)^2 \mathrm{d}R_0 \tag{19}$$

where R_0 is the size of one droplet and $\rho(R_0, t)$ represents the size distribution. This description is valid assuming the existence of only well-separated and spherical droplets in the microstructure. Although the shape derivation from a sphere in this system will induce error to a precise fitting of the data by Equation 19, the perfect isotropic pattern of scattering, as shown in

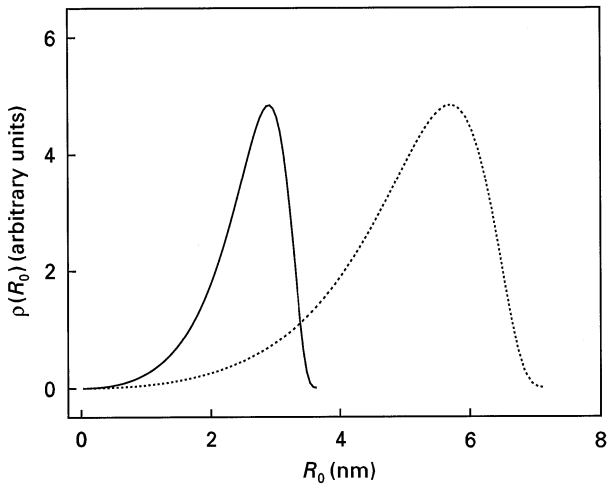

Figure 15 The evaluated size distribution, $\rho(R_0)$, of the supercooled liquid droplets in amorphous $Cu_{12.5}Ni_{10}Zr_{41}Ti_{14}Be_{22.5}$ annealed at $T = 620$ K for 860 min (——) and at $T = 643$ K for 870 min (- - - - -). R_0 is the radius of the droplet and the average sizes are 2.56 nm (——) and 5.03 nm. (- - - -).

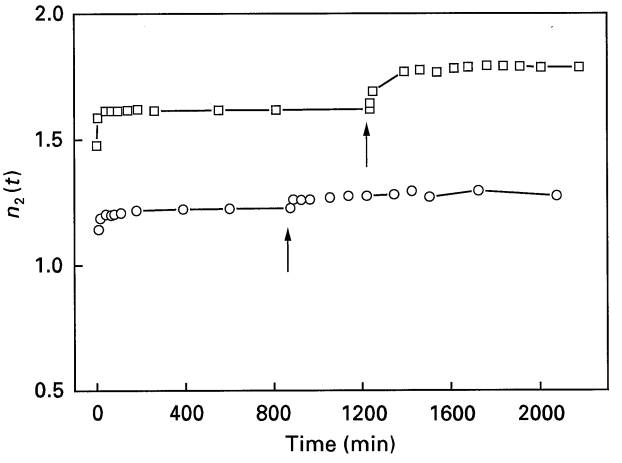

Figure 16 The scaling factor, n_2, plotted against time for the phase separation in amorphous $Cu_{12.5}Ni_{10}Zr_{41}Ti_{14}Be_{22.5}$ annealed at $T = 620$ K and then at $T = 673$ K (sample II) (□) and at $T = 643$ K and then $T = 673$ K (sample III) (○). The arrows indicate the times at which the temperature changed.

Fig. 1, still gives enough support for applying this equation.

We used the LSW-I and LSW-II models and the Gaussian model for obtaining $\rho(R_0, t)$. The LSW models are as follows [33]: for LSW-I,

$$\rho(R_0, t) = \varepsilon^2\left(\frac{3}{3+\varepsilon}\right)^{7/3}\left(\frac{1.5}{1.5-\varepsilon}\right)^{11/3} \times \exp\left(-\frac{\varepsilon}{1.5-\varepsilon}\right) \quad \varepsilon = \frac{R_0}{\bar{R}_0} \tag{20a}$$

if the growth kinetics are diffusion controlled and, for LSW-II,

$$\rho(R_0, t) = \varepsilon\left(\frac{2}{2-\varepsilon}\right)^5 \exp\left(-\frac{3\varepsilon}{2-\varepsilon}\right) \quad \varepsilon = \frac{R_0}{\bar{R}_0} \tag{20b}$$

if the growth kinetics are interface reaction controlled, where $\bar{R}_0$ is the average of R_0 with respect to this distribution.

The best fit was achieved for the data for the two temperatures using the LSW-1 model. The corresponding distributions at the two temperatures are presented in Fig. 15. First, we show that the phase separations in this alloy were diffusion controlled; secondly, compared with the LSW-II and Gaussian distributions, this distribution had much narrower full width at half-maximum, as previously predicted by the relatively regular correlation function shown in Fig. 10.

7. Dynamic scaling

For a diffusion-controlled phase separation sequence, the late-stage events should converge using the dynamic scaling if the interface-related excess energy is the unique driving force for microstructural coarsening. In this mode, the scaling state means that the distribution properties of the microstructure after being rescaled by its time-dependent characteristic length are stationary [36–38]. It would be interesting to check whether the phase separation sequence in this far from equilibrium alloy is dynamically scalable or not.

From Equation 6 we are able to derive the scaling factor $n_k(t)$:

$$n_k(t) = \frac{q_k(t)}{q_1^k(t)} \quad k = 1, 2, \ldots \tag{21}$$

The scaling theory predicts that, after this factor reaches a saturated state, the scattering functions can be scaled by applying the following transforms:

$$\Psi = \frac{q}{q_1(t)} \qquad F(\Psi) = \frac{q_1^3(t)S(q,t)}{S_D^2(t)} \tag{22}$$

where $F(\Psi)$ is called the universal scaling function.

Fig. 16 gives the calculated scaling factor, $n_2(t)$, as a function of time for the phase separations in the SLR and the following sequences at 673 K, involved in samples II and III, respectively. The arrows again indicate the times of temperature increase. In the SLR, the sequences at both 620 K and 643 K acquired a constant scaling factor after just annealing for tens of minutes. After these samples were heated to 673 K, a constant scaling factor was again achieved after the initial anneal for tens of minutes.

In Figs 17 and 18 are presented the scattering functions rescaled according to Equation 22, at several times for samples II and III annealed in the SLR and then at the crystallization point, 673 K. As predicted by Fig. 16, except for the events in the initial tens of minutes, all scattering functions in each of these sequences fall within the experimental uncertainties on the same curves, demonstrating that the scaling states were reached, separately, even in the early stage. It is then concluded that the phase separation in this multicomponent and highly supersaturated alloy does exhibit the dynamic scaling property. Note here that the

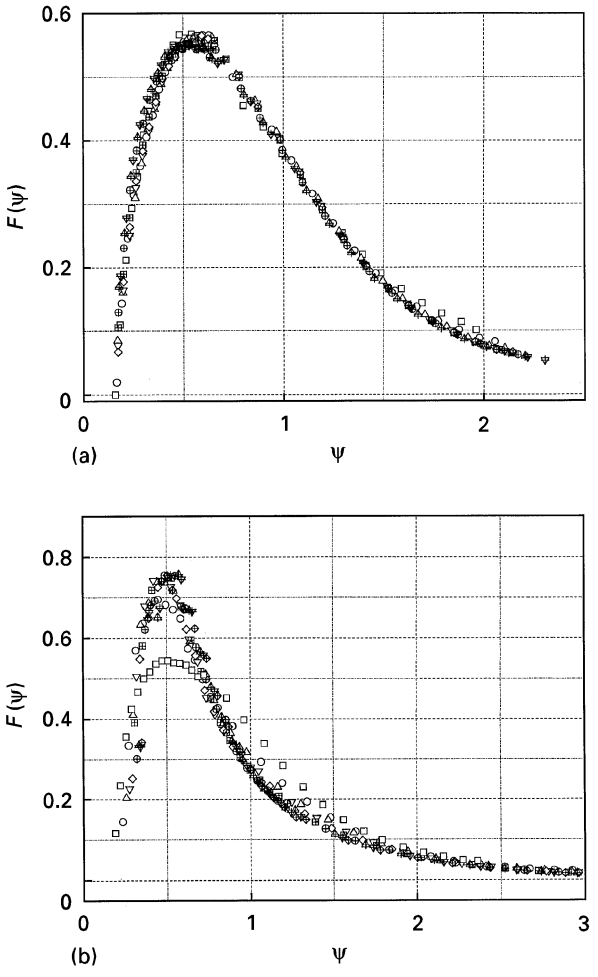

Figure 17 The rescaled scattering functions for phase separation in amorphous $Cu_{12.5}Ni_{10}Zr_{41}Ti_{14}Be_{22.5}$ (a) annealed at $T = 620$ K for various times ((□), 40 min; (○), 66 min; (△), 95 min; (▽), 140 min; (◇), 185 min; (⊞), 260 min; (⊕), 550 min; (◬), 810 min; (▽), 1236 min) and (b) then annealed at $T = 673$ K for various times ((□), 14 min; (○), 155 min; (△), 226 min; (▽), 380 min; (⊞), 443 min; (⊕), 527 min; (◬), 601 min; (▽), 675 min; (◈) 769 min).

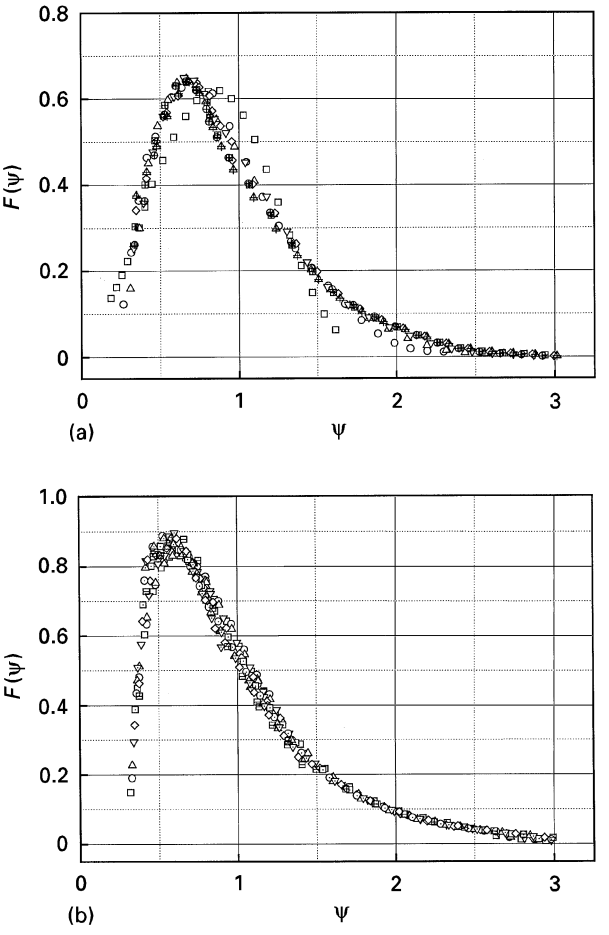

Figure 18 The rescaled scattering functions for phase separation in amorphous $Cu_{12.5}Ni_{10}Zr_{41}Ti_{14}Be_{22.5}$ (a) annealed at $T = 643$ K for various times ((□), 10 min; (○), 18 min; (△), 42 min; (▽), 80 min; (◇), 180 min; (⊞), 320 min; (⊕), 530 min; (◬), 875 min) and (b) then annealed at $T = 673$ K for various times ((□), 14 min; (○), 50 min; (△), 90 min; (▽), 180 min; (◇), 264 min; (⊡), 347 min; (⊙), 470 min; (◬), 550 min; (▽), 630 min; (◇), 850 min; (⊟), 1200 min).

different sequences acquired for different scaling curves, which cannot be described by a unique scaling function.

8. Conclusions

In conclusion, we have presented a detailed investigation of the phase separation in amorphous $Cu_{12.5}Ni_{10}Zr_{41}Ti_{14}Be_{22.5}$ alloy and its effect on subsequent crystallization, by means of SANS. The following conclusions have been made.

1. The phase separation sequence has been detected over all the SLR of this alloy. The observed SANS spectrum was perfectly isotropic. There was no crystallization detected in the SLR within the scale used in the present experiment (about 20 h). However, no phase separation occurred besides crystallization as the homogeneous alloy was annealed around and above the crystallization point (673 K).

2. The structural relaxation via phase separation in the SLR promoted significant thermal stability of the alloy against crystallization, by slowing down the kinetics of crystallization. The lower the temperature at which the alloy was fully relaxed in the SLR, the higher the thermal stability was. In the alloy previously relaxed in the SLR, in parallel to crystallization a further phase separation sequence was initiated. However, this new sequence may result in a significantly different microstructure, depending on the thermal path of the alloy in the SLR.

3. The phase separation developed rapidly in the early stage, leaving a sluggish coarsening stage. The microstrucure consisted of a droplet-like supercooled liquid phase embedded in a matrix of another supercooled liquid and showed a considerable temperature dependence. The droplet-like phase acquired a relatively regular distribution and a low volume fraction (10–16%). The droplet morphology was evaluated to be bar-like but not spherical.

4. It has been demonstrated that the phase separation developed via the spinodal mode. The kinetic exponent for the late-stage coarsening in the SLR was only about 0.06 and increased to higher values for sequences subsequent the crystallization point. These exponents were much lower than the LSW exponent, owing to the continuously decreasing diffusivity of some elements. The size of the liquid droplets formed in the SLR increased linearly with increasing

temperature. These droplets followed the LSW-I-type size distribution.

5. Except for the initial tens of minutes, a universal scaling of the scattering functions was achieved for all the phase separation sequences, demonstrating the dynamic scaling property of phase separation in this highly supercooled alloy.

Acknowledgements

The author would like to thank the Alexander von Humboldt-Stiftung of Germany for the financial support of this work. Valuable comments and suggestions from Dr A. Wiedenmann, Dr M.-P. Macht, Mr U. Gerold, Dr N. Wanderka, Ms Q. Wei and Professor H. Wollenberger are acknowledged.

References

1. W. KLEMENT, R. WILLENS and P. DUWEZ, Nature **187** (1960) 869.
2. D. TURNBUL, *Contemp. Phys.* **10** (1969) 473.
3. T. MASUMOTO and K. SUZUKI (eds), "Rapidly quenched metals IV" (Japan Institute of Metals, Sendai, 1981).
4. F. E. LUBORSKY (ed.), 'Metallic alloys" (Butterworth, London, 1983).
5. S. STEEB and H. WARLIMONT (eds), "Rapidly quenched metals VI" (Elsevier, Amsterdam, 1985).
6. T. MASUMOTO, *Bull. Jpn Inst. Metals* **30** (1991) 375.
7. A. INOUE, T.ZHANG and T. MASUMOTO, *Mater. Trans. Jpn Inst Metals* **31** (1990) 177.
8. A. L. GREER, *Nature* **366** (1993) 6453.
9. T. MASUMOTO, *Sci. Rep. Res. Instr., Tohoku Univ. A* **39** (1994) 91.
10. A. INOUE, T. ZHANG and T. MASUMOTO, *Mater. Trans. Jpn Inst. Metals* **36** (1995) 391.
11. W. L. JOHNSON and A. PEKER, in "Science and technology of rapid solidification and processing", edited by M. A. Otooni (Kluwer, Deventer, 1995) p. 25.
12. A. PEKER and W. L. JOHNSON, *Appl. Phys. Lett.* **63** (1993) 2342.
13. Y. J. KIM, R. BUSCH, W. L. JOHNSON, A. J. RULISON and W. K. RHIM, *Appl. Phys. Lett.* **65** (1994) 2136.
14. R. BUSCH, Y. J. KIM, W. L. JOHNSON, A. J. RULISON, W. K. RHIM and D. ISHEIM, *ibid.* **66** (1995) 3111.
15. U. GEYER, S. SCHNEIDER, W. L. JOHNSON, A. J. RULISON, Y. QIU, T. A. TOMBRELLO and M. P. MACHT, *Phys. Rev. Lett.* **75** (1995) 2354.
16. R. BUSCH, S. SCHNEIDER, A. PEKER and W. L. JOHNSON, *Appl. Phys. Lett.* **67** (1995) 1544.
17. S. G. KLOSE, PhD thesis, Herbert Utz Verlag Wissenschaft, München (1995).
18. S. SCHNEIDER, P. THIYAGARAJAN and W. L. JOHNSON, *Appl. Phys. Lett.* **68** (1996) 493.
19. M. P. MACHT, N. WANDERKA, A. WIEDENMANN, H. WOLLENBERGER, Q. WEI, H. J. FECHT and S. G. KLOSE, *Mater. Sci. Forum* **225/227** (1996) 65.
20. A. WIEDENMANN, U. KEIDERLING, M. P. MACHT and H. WOLLENBERGER, *Mater. Sci. Forum* **225/227** (1996) 71.
21. L. E. TANNER and R. RAY, *Script Metall.* **14** (1986) 657.
22. D. DENG and A. S. ARGON, *Acta Metall.* **10** (1986) 2011.
23. R. BORMANN, F. GÄRTNER and F. HAIDER, *Mater. Sci. Engng* **97** (1988) 79.
24. A. H. OKUMURA, A. INOUE and T. MASUMOTO, *Acta Metall. Mater.* **41** (1993) 915.
25. E. BUDKE, P. FIELITZ, M. P. MACHT, V. NAUNDORF and G. FROHBERG, in "Proceedings of the International Conference on Diffusion in Materials", edited by H. Mehrer (Tarnstec, Winterthur, 1997) in press.
26. U. KEIDERLING and A. WEIDENMANN, *Physica B* **213** (1995) 895.
27. O. GLATTER and O. KRATKY, "Small angle X-ray scattering" (Academic Press, London, 1982).
28. H. FURUKAWA, *Physica A* **123** (1984) 497.
29. C. YEUNG, *Phys. Rev. Lett.* **61** (1988) 1135.
30. C. E. WILLIAMS, R. P. MAY and A. GUINIER, in "Materials science and technology: a comprehensive treatment", Vol. 2B, edited by R. W. Cahn, P. Haasen and E. J. Kramer (VCH, Weinheim, 1993) p. 612.
31. P. FRATZL and J. L. LEBOWITZ, *Acta Metall. Mater.* **37** (1989) 3245.
32. F. LANGMAYR, P. FRATZL and G. VOGEL, *ibid.* **40** (1992) 3381.
33. I. M. LIFSHITZ and V. V. SLYOZOV, *J. Phys. Chem. Solids* **19** (1961) 35.
34. N. E. SLUCHANKO, V. V. GLUSHKOV, N. A. SAMARIN and V. V. BRAZHKIN, *Phys. Rev. B* (1997) in press.
35. P. FRATZL and O. BLASCHKO, in "Dynamics of ordering processes in condensed matter", edited by S. Komura and H. Furukawa (Plenum, New York, 1987) p. 223.
36. H. FURUKAWA, *Adv. Phys.* **34** (1985) 703.
37. A. CRAEVICH and J. M. SANCHEZ, *Phys. Rev. Lett.* **18** (1981) 1308.
38. K. BINDER and D. W. HEERMANN, in "Scaling phenomena in disordered systems", edited by R. Pynn and A. Skjeltorp (Plenum, New York, 1985) p. 207.

Received 5 July 1996
and accepted 10 March 1997